

Accelerated adiabatic passage of a single electron spin qubit in quantum dots

Xiao-Fei Liu^{1,2,*}, Yuta Matsumoto¹, Takafumi Fujita¹, Arne Ludwig³, Andreas D. Wieck³ and Akira Oiwa^{1,4,5,6,†}

¹SANKEN, Osaka University, 8-1 Mihogaoka, Ibaraki, Osaka 567-0047, Japan

²Beijing Academy of Quantum Information Sciences, Beijing 100193, China

³Lehrstuhl für Angewandte Festkörperphysik, Ruhr-Universität Bochum, Universitätsstraße 150, Gebäude NB, D-44780 Bochum, Germany

⁴Center for Quantum Information and Quantum Biology (QIQB), Osaka University, Osaka 565-0871, Japan

⁵Center for Spintronics Research Network (CSRN),

Graduate School of Engineering Science, Osaka University, Osaka 560-8531, Japan

⁶Spintronics Research Network Division, OTRI, Osaka University, Osaka 565-0871, Japan

Adiabatic processes can keep the quantum system in its instantaneous eigenstate, which is robust to noises and dissipation. However, it is limited by sufficiently slow evolution. Here, we experimentally demonstrate the transitionless quantum driving (TLQD) of the shortcuts to adiabaticity in gate-defined semiconductor quantum dots (QDs) to greatly accelerate the conventional adiabatic passage for the first time. For a given efficiency of quantum state transfer, the acceleration can be more than twofold. The dynamic properties also prove that the TLQD can guarantee fast and high-fidelity quantum state transfer. In order to compensate for the diabatic errors caused by dephasing noises, the modified TLQD is proposed and demonstrated in experiment by enlarging the width of the counterdiabatic drivings. The benchmarking shows that the state transfer fidelity of 97.8% can be achieved. This work will greatly promote researches and applications about quantum simulations and adiabatic quantum computation based on the gate-defined QDs.

Introduction.— Gate-defined semiconductor quantum dots (QDs) can electrically control electron and hole states with ultrahigh precision, which is one of the state-of-the-art quantum devices [1, 2]. The spin qubit of QDs is a promising candidate for fault-tolerant solid-state quantum computing due to its high-fidelity quantum operation [3–6], potential scalability [7–9], and well compatibility with manufacturing technology of semiconductor industry [10]. Recently, two-qubit gate fidelity of more than 99% has been demonstrated experimentally [11–14], crossing the well-known surface code threshold [15, 16]. Besides, QD systems are becoming emerging platforms for quantum simulations to explore strongly interacting electrons and topological phases in condensed-matter physics, such as the Fermi–Hubbard system [17], Nagaoka ferromagnetism [18], and the Su–Schrieffer–Heeger model [19].

In order to achieve the so called “quantum advantage” [20], a high-fidelity quantum processor with large enough computational space and programmable qubits is required. Meanwhile, it also needs accurate quantum control and good robustness against noises and dissipation. One possible pathway is to find a feasible quantum control theory that is applicable for the large-scale quantum processor and guarantees high-accuracy quantum operation simultaneously. It is well known that the manipulation of a quantum state using resonant pulses is sensitive to timing and pulse area errors. In contrast, adiabatic passage can always keep some properties of a dynamical quantum system invariant, ideally switching

an initial state into the target state, such as the high fidelity adiabatic process demonstrated in ³¹P electron qubit of silicon QD system [21]. This can well prevent decoherence from experimental imperfections [22]. Generally, slow enough evolution is necessary to satisfy adiabatic conditions, limiting its applications. To achieve rapid and robust quantum state manipulation, several shortcuts to adiabaticity (STA) schemes are put forward to compensate for the nonadiabatic errors [23–27], for instance the transitionless quantum driving (TLQD) and invariant-based inverse engineering. Some of them have been demonstrated in other quantum systems [28–33]. Besides, STA has significant applications in quantum simulations to greatly suppress diabatic excitations [34].

Here, we experimentally demonstrate the STA of a single spin qubit in gate-defined QDs for the first time. The experiment is based on the theory of TLQD [23], and the acceleration of quantum state transfer has been achieved. This is also verified from the dynamics of the spin state. To suppress the noises from nuclear spin fluctuations, we propose and experimentally demonstrate a modified TLQD (MOD-TLQD) by enlarging the width of the counterdiabatic pulse. The benchmarking of this MOD-TLQD demonstrates a state transfer efficiency of 97.8%. Since the gate-defined QDs are moving toward the scalable quantum processor [35], the results of this paper will greatly promote related researches about quantum control and quantum simulations.

The acceleration of quantum state transfer.— Figure 1(a) shows a scanning electron microscope picture of the double QDs (DQDs), which are fabricated on the GaAs/AlGaAs heterostructure. After the implementation of an in-plane magnetic field B_{ext} , the qubit frequency of a single electron spin is $f_{\text{qubit}} = |g|\mu_B B / (2\pi\hbar)$,

* liuxf@baqis.ac.cn

† oiwa@sanken.osaka-u.ac.jp

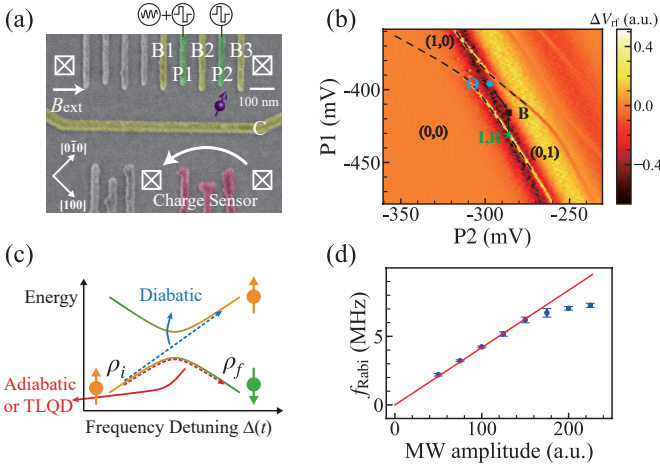


Figure 1. The device and its basic properties. (a) The false-colored micrograph of the device. The high frequency pulses are applied through the plunger gates P1 and P2, and the MW driving is connected with P1. (b) Charge stability diagram around single electron region. The position of I, B, and O are represented by the green star, black square, and blue circle, respectively. The position of the initialization is also used for the readout. (c) The schematic of TLQD. (d) Rabi frequency f_{Rabi} as a function of the MW amplitude. Its maximum value is about $f_{\text{Rabi}}^{\text{max}} \sim 7.5$ MHz.

in which μ_B is the Bohr magneton, g is the Landé g -factor (~ -0.41 for this GaAs QDs), and B is the total magnetic field (consists of B_{ext} and the effective Overhauser field B_{nuc}^z). When a microwave (MW) driving is applied, the spin manipulation can be achieved using electric dipole spin resonance [36]. Besides, we use interdot tunneling to enhance the Rabi frequency [37]. We employ energy-selective readout to measure the spin state [38–40]. A nearby charge sensor provides rapid and real time detection of charge state based on the radio frequency (RF) reflectometry [41, 42].

Under the rotating frame, the interaction Hamiltonian expanded on the $|\uparrow\rangle$ and $|\downarrow\rangle$ Hilbert space is

$$\hat{H}_0 = \frac{\hbar}{2} \begin{pmatrix} -\Delta(t) & \Omega_R(t) \\ \Omega_R(t) & \Delta(t) \end{pmatrix}, \quad (1)$$

in which $\Omega_R(t)$ is the Rabi frequency, and $\Delta(t)$ is the frequency detuning with the expression $\Delta(t) = \omega_{\text{qubit}} - \omega_{\text{MW}} - t\dot{\omega}_{\text{MW}}$. A high-fidelity quantum state transfer can occur if the evolution of this controllable parameter $\Delta(t)$ is slow enough. However, the TLQD can correct diabatic errors by adding the counterdiabatic driving \hat{H}_{CD} even though the evolution does not satisfy adiabatic conditions [23], as shown in Fig. 1(c). The TLQD can always keep the system in $|\varphi_k(t)\rangle$, the instantaneous eigenstate of \hat{H}_0 . Therefore, the time-dependent evolution operator and total Hamiltonian can be obtained. Furthermore, we can know \hat{H}_{CD} which has the expression $i\hbar \sum_k |\partial_t \varphi_k\rangle \langle \varphi_k|$. For this single electron spin system, its specific expression is $\hat{H}_{\text{CD}} = \hbar \Omega_a(t) \sigma_y / 2$,

in which $\Omega_a(t) = [\Omega_R(t) \dot{\Delta}(t) - \dot{\Omega}_R(t) \Delta(t)] / \Omega^2$ and $\Omega^2 = \Delta^2(t) + \Omega_R^2(t)$. Obviously, the function of \hat{H}_{CD} is to correct the diabatic errors by applying a time-dependent driving in \hat{y} -axis.

In our experiment, the electron is initialized to $|\uparrow\rangle$ state at the initialization point (I), as shown in Fig. 1(b). Then, the pulse sequences applied on plunger gates P1 and P2 deliver this electron to the intermediate transit point (B) and then to the operation point (O). After the spin manipulation at O point, this electron is delivered back to B and then to the readout point (R). Here, I and R points are the same. Our setup utilizes an arbitrary waveform generator and an I/Q mixer to precisely tune the time-dependent terms Ω_R , Ω_a , and Δ . The relationship between Ω_R (or Ω_a) and the MW amplitude has to be characterized firstly. The Rabi frequency estimated from the Rabi oscillation and Landau-Zener transition are nearly the same. Please find more details in Section III of the Supplementary Materials. As shown in Fig. 1(d), f_{Rabi} increases linearly with larger MW amplitude. Then, it becomes saturated progressively until reaching the maximum value $f_{\text{Rabi}}^{\text{max}} \sim 7.5$ MHz because of the limitation from the trapping potentials or MW amplifiers.

The most significant advantage of this TLQD is that it can always guarantee a quantum system in one of its instantaneous eigenstates and greatly accelerate the adiabatic passage. Figure 2(a) shows the final spin down probability P_{\downarrow} and state transfer efficiency (or fidelity) F_{flip} as a function of the total evolution time T_e . The green squares and blue circles represent the results of TLQD and conventional adiabatic evolution, respectively. The red solid line is the least-squares fitting to the Landau-Zener formula [43–45]. The experimental results show that TLQD always has higher P_{\downarrow} and F_{flip} than the conventional adiabatic passage. The differences of P_{\downarrow} (also F_{flip}) between TLQD and adiabatic passage become smaller progressively with longer T_e (slower evolution speed). When T_e is long enough, Ω_a becomes small enough to be neglected, in analogy to the adiabatic evolution. Note that F_{flip} is evaluated from the experimental results P_{\downarrow} by taking the initialization fidelity ($F_{\text{ini}}^{\uparrow}$), spin-to-charge fidelity ($F_{\text{STC}}^{\downarrow}$ and $F_{\text{STC}}^{\uparrow}$), and charge detection fidelity (F_{E}) into consideration. Please check Section I and VI in the Supplementary Materials. Generally, the relationship $P_{\downarrow} = P_{\downarrow}^{\text{ini}=\uparrow} + P_{\downarrow}^{\text{ini}=\downarrow}$ exists, in which $P_{\downarrow}^{\text{ini}=\uparrow}$ and $P_{\downarrow}^{\text{ini}=\downarrow}$ stand for the situations with the initialization of spin to up and down state, respectively. The expressions of $P_{\downarrow}^{\text{ini}=\uparrow}$ and $P_{\downarrow}^{\text{ini}=\downarrow}$ are $F_{\text{ini}}^{\uparrow} F_{\text{flip}} F_{\text{STC}}^{\downarrow} F_{\text{E}} + F_{\text{ini}}^{\uparrow} (1 - F_{\text{flip}}) (1 - F_{\text{STC}}^{\uparrow}) F_{\text{E}}$ and $(1 - F_{\text{ini}}^{\uparrow}) (1 - F_{\text{flip}}) F_{\text{STC}}^{\downarrow} F_{\text{E}} + (1 - F_{\text{ini}}^{\uparrow}) F_{\text{flip}} (1 - F_{\text{STC}}^{\uparrow}) F_{\text{E}}$, respectively. We also make sure that the enhancement of state transfer originates from the compensation for diabatic errors instead of simply enlarging the Rabi frequency, please see Section II in the Supplementary Materials. In our experiment, the maximum value of P_{\downarrow} is about 0.85, which is mainly limited by the readout fidelity. It can be improved by enhancing the relaxation

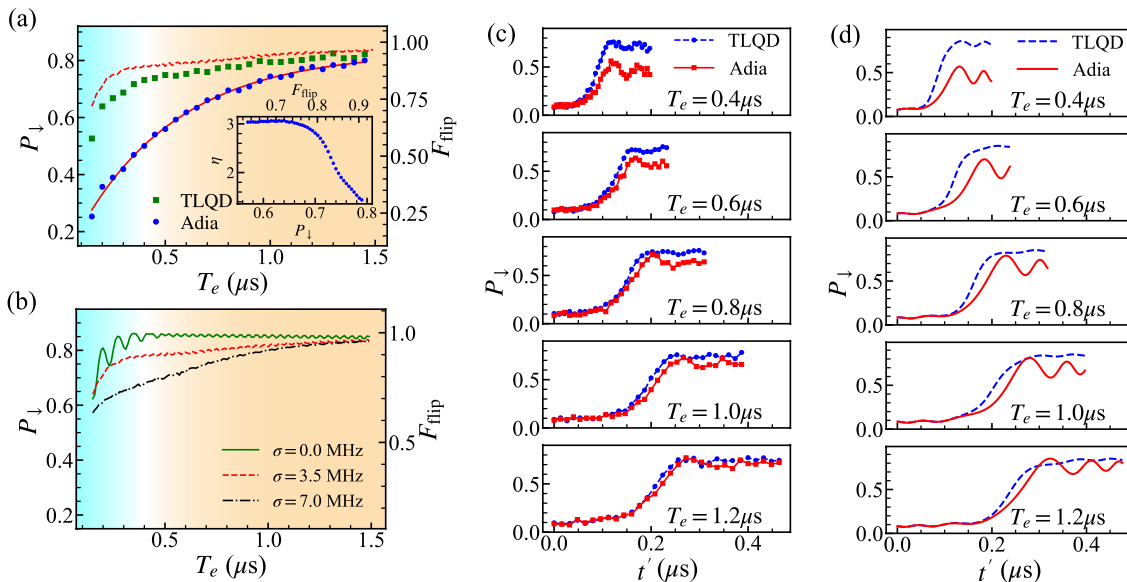


Figure 2. The result of TLQD. (a) The final spin down probability P_{\perp} as a function of the evolution time T_e using the conventional adiabatic evolution and TLQD. The red solid line is the fitting to the formula $AP_{\perp}^{LZ} + B$, giving the value of $\Omega_R/2\pi = 4.63$ MHz. The inset displays the speedup factor η as functions of P_{\perp} and the efficiency of state transfer F_{flip} . (b) The simulation results of P_{\perp} and F_{flip} as a function of T_e under different variance of qubit frequency noise $\sigma \sim 0.0$ (green solid line), 3.5 (red dashed line), and 7.0 MHz (black dash-dotted line). To better compare the simulation and experimental results, the red dashed line with $\sigma \sim 3.5$ MHz is also plotted in (a). The modulation depth is $\delta_d = 100.0$ MHz. The maximum Rabi frequency is assumed to be $f_{\text{Rabi}}^{\text{max}} = 7.5$ MHz. (c) and (d) are the experimental and simulation results of the dynamics of P_{\perp} , respectively. The Rabi frequency is $\Omega_R/2\pi = 4.18$ MHz.

time T_1 and bandwidth of the RF-reflectometry after demodulation.

We find that P_{\perp} and F_{flip} of TLQD decrease more rapidly when $T_e < 0.4 \mu\text{s}$. This originates from the saturation of Ω_a (because of the large compensation for diabatic errors and the limited value of $f_{\text{Rabi}}^{\text{max}}$). Please find the simulation results without considering the limitation of $f_{\text{Rabi}}^{\text{max}}$ in Fig. S13 of the Supplementary Materials. When $T_e > 0.4 \mu\text{s}$, there is a tiny increase of P_{\perp} and F_{flip} . As you can see in Section II of the Supplementary Materials, the TLQD has the highest efficiency of state transfer when $f_{\text{qubit}} = f_{\text{MW}}^c$ (f_{MW}^c is the center frequency of the MW). The dephasing noises (mainly from the Overhauser field) would cause the fluctuations of B_{nuc}^z and degrade the performance of TLQD.

The simulation after taking dephasing noises and saturation of Rabi frequency into consideration is also performed. For the GaAs QDs [46, 47], the coherence time is dominated by the quasistatic (or low-frequency) noises with a spectral distribution $S(f) \propto 1/f^{\beta}$. For simplicity, β is set to be 2; i.e., $S(f) = A^2/f^2$. The variance of the qubit frequency σ can be estimated as $\sigma^2 = 2 \int_{f_c}^{1/t} S(f) df = 2A^2(1/f_c - t)$. Here, f_c and $1/t$ are low and high cutoff frequencies, respectively. The value of A can be calculated from the Ramsey pattern. Using the relationship $1/T_2^* = \sqrt{2}\pi\sigma$, we know $1/T_2^* = 2\pi A\sqrt{1/f_c - t}$. Please find more details in Section V of the Supplementary Materials. Here, the satu-

ration value of total Rabi frequency is $f_{\text{Rabi}}^{\text{max}} = 7.5$ MHz, i.e., $\Omega(t)$ is set as 7.5 MHz if $\Omega(t) > f_{\text{Rabi}}^{\text{max}}$. The value of σ is about 3.5 MHz. The simulation result is plotted as the red dashed line in both Figs. 2(a) and 2(b), which can well reproduce experimental results qualitatively. For GaAs QDs, β may range between 1 and 3. This just changes the value of A without changing the estimation of σ too much. In our simulation, we generate 2000 random values of δf_{qubit} (the shift of the qubit frequency) with the variance σ . For each δf_{qubit} , we can know F_{flip} (also P_{\perp} based on the relationship with F_{flip}) by solving the Schrödinger equation of $\hat{H}_0 + \hat{H}_{\text{CD}}$. The average values of F_{flip} and P_{\perp} are the simulation results.

Generally, the TLQD consumes less time compared with conventional adiabatic evolution for a given state transfer efficiency. This acceleration can be characterized quantitatively by the time ratio $\eta = T_{\text{adia}}/T_{\text{TLQD}}$, in which T_{TLQD} and T_{adia} represent the time using the TLQD and conventional adiabatic passage, respectively. The result is shown in the inset of Fig. 2(a), in which an acceleration of more than twofold can be achieved. The value of η becomes flat when $P_{\perp} < 0.65$, which is due to the limitation of $f_{\text{Rabi}}^{\text{max}}$. Note that T_{TLQD} is estimated from the polynomial fitting to the experimental results of TLQD, and T_{adia} is deduced from the fitting to the Landau-Zener formula. We believe that the acceleration would be much faster for QDs with longer coherence time, e.g., silicon QDs [48]. The green solid line in Fig. 2(b)

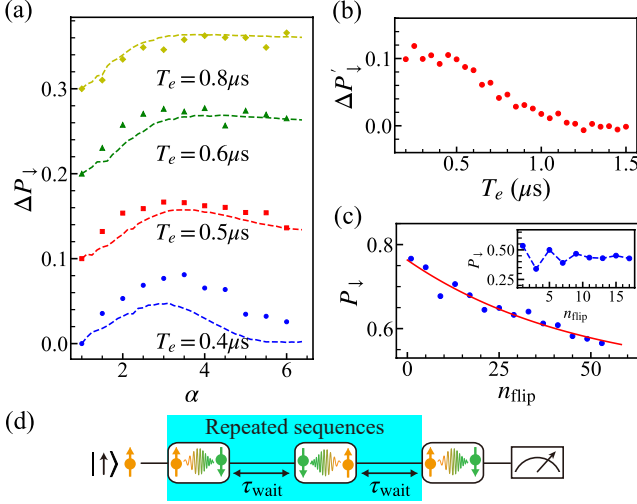


Figure 3. The result of MOD-TLQD. (a) The enhancement of spin flip probability ΔP_{\downarrow} as a function of α under different T_e . The markers are experimental data, and the lines represent simulation results. The variance of qubit frequency is $\sigma \sim 2.9$ MHz. The traces are shifted vertically for clarity. (b) The enhancement of spin flip probability $\Delta P'_{\downarrow}$ as a function of T_e . The width factor is set to be $\alpha = 2.5$. The Rabi frequency in (a) and (b) is $\Omega_R/2\pi \sim 4.0$ MHz. (c) The benchmarking of the efficiency of state transfer using the MOD-TLQD, giving the value of $p = 0.978 \pm 0.01$. The inset corresponds to the result of conventional adiabatic evolution, which has the oscillation instead of an exponential decay. (d) The schematic of pulse sequences to benchmark the spin flip fidelity.

shows the simulation results if $\sigma = 0.0$ MHz. When the evolution time $T_e > 0.4 \mu\text{s}$, P_{\downarrow} and F_{flip} can always keep the highest value. Furthermore, an acceleration of $\eta > 6$ can be achieved from our rough estimation. In contrast, large noises would greatly lower the efficiency of state transfer, represented by the black dash-dotted line.

The dynamic properties of TLQD and adiabatic evolution are also investigated experimentally, as shown in Fig. 2(c). The blue line with circle dots and red line with square dots represent the results of TLQD and conventional adiabatic evolution, respectively. Here, we just show the results starting from the time $0.3 T_e$, i.e., the relative time t' has a shift of $0.3 T_e$ with respect to the real time. Simulation results are displayed in Fig. 2(d), which can well reproduce experimental results. The experimental and simulation results show that this TLQD can always keep highest P_{\downarrow} (also F_{flip}) after spin flip under various T_e ranging from $0.4 \mu\text{s}$ to $1.2 \mu\text{s}$. In contrast, P_{\downarrow} (also F_{flip}) would increase gradually with longer T_e for the conventional adiabatic evolution. Meanwhile, its P_{\downarrow} has much larger amplitude of oscillation compared with TLQD after the spin flip because its quantum state is not the eigenstate of this system.

Compensation for dephasing noises.— For an ideal case, the efficiency of state transfer using TLQD can be up to 100%. There are two main reasons that make it dif-

ficult to realize such high efficiency. The first comes from charge noises, which may cause a shift of the O point and Ω_R , leading to the over- or underestimated value of Ω_a . The second is the nuclear spin fluctuations, which can cause the shift of qubit frequency and significant dephasing in GaAs QDs. Here, we propose a feasible and simple method through pulse optimization to greatly compensate for dephasing noises.

In the TLQD experiment demonstrated above, Ω_R is kept as a constant and Δ is modulated linearly. Therefore, Ω_a has a Gaussian envelope, i.e., $\Omega_a(t) \propto (\Delta^2 + \Omega_R^2)^{-1}$. In order to compensate for the dephasing noises, we can enlarge the width of this Gaussian envelope without changing the maximum value of Ω_a . This modified pulse is $\Omega_a^{\text{MOD}}(t) = \alpha^2 \Omega_R \dot{\Delta} (\Delta^2 + \alpha^2 \Omega_R^2)^{-1}$. Here, α is the width factor, and this optimization makes the pulse width to be $\alpha \Omega_R$. The enhancement of P_{\downarrow} , with the definition $\Delta P_{\downarrow}(\alpha) = P_{\downarrow}(\alpha) - P_{\downarrow}(\alpha = 1.0)$, as a function of α under various T_e is shown in Fig. 3(a). It shows that P_{\downarrow} would increase with α firstly and reach the maximum when α ranges from 2.5 to 3.0. If $T_e < 0.6 \mu\text{s}$, there is a clear drop of ΔP_{\downarrow} when $\alpha > 2.5$, which may be due to the overcompensation for diabatic errors. In contrast, ΔP_{\downarrow} is nearly flat when $\alpha > 2.5$ for the situation of $T_e > 0.6 \mu\text{s}$. The reason is that Ω_a becomes smaller and the effect of overcompensation is not obvious any more. The simulation results shown as the dashed lines can well reproduce our experimental results. We also note that the simulation result of $T_e = 0.4 \mu\text{s}$ is much smaller than the experimental result, which may be due to the underestimated value of $f_{\text{Rabi}}^{\text{max}}$ in our calculation.

In order to well demonstrate the performance of this width optimization method, the enhancement of P_{\downarrow} defined as $\Delta P'_{\downarrow} = \Delta P_{\downarrow}(\alpha = 2.5)$ as a function of T_e is displayed in Fig. 3(b). There is a clear enhancement under various T_e . Thus, the degradation of state transfer caused by the dephasing noises can be greatly compensated using the MOD-TLQD. Meanwhile, $\Delta P'_{\downarrow}$ becomes smaller progressively with longer T_e because of the negligible Ω_a . When $T_e > 1.1 \mu\text{s}$, $\Delta P'_{\downarrow}$ is nearly zero. Besides, the optimal value of α will become smaller with larger Ω_R because we have to keep $\alpha \Omega_R$ comparable with the dephasing noises. Please see more data in Section VIII of the Supplementary Materials.

Finally, the performance of this MOD-TLQD is characterized quantitatively. The probability P_{\downarrow} as a function of the spin flip number n_{flip} is measured, as shown in Fig. 3(c). The evolution time is $T_e = 0.6 \mu\text{s}$, and a waiting time $\tau_{\text{wait}} = 0.2 \mu\text{s}$ is added after each spin flip process to reduce the thermal heating, as shown in Fig. 3(d). The repeated sequences represent two flips in a row to keep the spin up state. After fitting to the formula $P_{\downarrow} = Ap^{n_{\text{flip}}} + B$, the fidelity $p = 0.978 \pm 0.01$ is obtained. The relationship between n_{flip} and the number of this repeated sequences n_{seq} is $n_{\text{flip}} = 2n_{\text{seq}} + 1$. In contrast, the conventional adiabatic evolution has a clear oscillation for $T_e = 0.6 \mu\text{s}$, as shown in the inset in Fig. 3(c). Only when T_e is large enough (larger than $1.1 \mu\text{s}$), the ex-

ponential decay can be observed. More data can be found in Fig. S12 of the Supplementary Materials. If we perform the spin flip using Rabi oscillation under the same conditions with Fig. 3(a), i.e., $\Omega_R/2\pi = 4.0$ MHz and $\sigma = 2.9$ MHz, the spin flip fidelity is less than 65.6%. Therefore, MOD-TLQD has higher fidelity, although it takes longer time.

Conclusion and outlook.— The STA is experimentally demonstrated in gate-defined QDs for the first time based on the TLQD protocol. Furthermore, the optimization by enlarging the width of counterdiabatic driving can achieve the efficiency of state transfer as high as 97.8%. The acceleration of quantum state transfer would be much better in Si or Ge QDs with longer coherence time. We also find that the experimental method in our paper can be directly used in the invariant-based inverse engineering [25], which also needs the precise control

of time-dependent terms $\Delta(t)$, $\Omega_R(t)$, and $\Omega_a(t)$. Besides, for the cases that the input is a superposition state, i.e., $(|\uparrow\rangle + |\downarrow\rangle)/\sqrt{2}$, the output state would become $(|\uparrow\rangle - |\downarrow\rangle)/\sqrt{2}$. It means a π rotation along the \hat{z} -axis for this superposition state. Meanwhile, the TLQD may be used in other single-qubit operations and adiabatic passages of the QDs system. However, it still needs more researches in both theory and experiment.

This work is supported by JST CREST Grant No. JPMJCR15N2; JST Moonshot R&D Grant No. JPMJMS2066-31 and JPMJMS226B; QSP-013 from NRC, Canada; and the Dynamic Alliance for Open Innovation Bridging Human, Environment and Materials. A. L. and A. D. W. acknowledge the support of DFG-TRR160 and BMBF-QR.X Project 16KISQ009.

-
- [1] D. Loss and D. P. DiVincenzo, “Quantum computation with quantum dots,” *Phys. Rev. A* **57**, 120 (1998).
- [2] R. Hanson, L. P. Kouwenhoven, J. R. Petta, S. Tarucha, and L. M. K. Vandersypen, “Spins in few-electron quantum dots,” *Rev. Mod. Phys.* **79**, 1217 (2007).
- [3] M. Veldhorst, J. C. C. Hwang, C. H. Yang, A. W. Leenstra, B. de Ronde, J. P. Dehollain, J. T. Muhonen, F. E. Hudson, K. M. Itoh, A. Morello *et al.*, “An addressable quantum dot qubit with fault-tolerant control-fidelity,” *Nat. Nanotechnol.* **9**, 981 (2014).
- [4] M. Veldhorst, C. H. Yang, J. C. C. Hwang, W. Huang, J. P. Dehollain, J. T. Muhonen, S. Simmons, A. Laucht, F. E. Hudson, K. M. Itoh, A. Morello, and A. S. Dzurak, “A two-qubit logic gate in silicon,” *Nature* **526**, 410 (2015).
- [5] J. Yoneda, K. Takeda, T. Otsuka, T. Nakajima, M. R. Delbecq, G. Allison, T. Honda, T. Koderu, S. Oda, Y. Hoshi *et al.*, “A quantum-dot spin qubit with coherence limited by charge noise and fidelity higher than 99.9%,” *Nat. Nanotechnol.* **13**, 102 (2018).
- [6] J. M. Nichol, L. A. Orona, S. P. Harvey, S. Fallahi, G. C. Gardner, M. J. Manfra, and A. Yacoby, “High-fidelity entangling gate for double-quantum-dot spin qubits,” *npj Quantum Inf.* **3**, 3 (2017).
- [7] D. M. Zajac, T. M. Hazard, X. Mi, E. Nielsen, and J. R. Petta, “Scalable Gate Architecture for a One-Dimensional Array of Semiconductor Spin Qubits,” *Phys. Rev. Appl.* **6**, 054013 (2016).
- [8] L. M. K. Vandersypen, H. Bluhm, J. S. Clarke, A. S. Dzurak, R. Ishihara, A. Morello, D. J. Reilly, L. R. Schreiber, and M. Veldhorst, “Interfacing spin qubits in quantum dots and donors—hot, dense, and coherent,” *npj Quantum Inf.* **3**, 34 (2017).
- [9] R. Li, L. Petit, D. P. Franke, J. P. Dehollain, J. Helsen, M. Steudtner, N. K. Thomas, Z. R. Yoscovits, K. J. Singh, S. Wehner *et al.*, “A crossbar network for silicon quantum dot qubits,” *Sci. Adv.* **4**, eaar3960 (2018).
- [10] A. M. J. Zwerver, T. Krähenmann, T. F. Watson, L. Lampert, H. C. George, R. Pillarisetty, S. A. Bojarski, P. Amin, S. V. Amitonov, J. M. Boter *et al.*, “Qubits made by advanced semiconductor manufacturing,” *Nat. Electron.* **5**, 184 (2022).
- [11] X. Xue, M. Russ, N. Samkharadze, B. Undseth, A. Sammak, G. Scappucci, and L. M. K. Vandersypen, “Quantum logic with spin qubits crossing the surface code threshold,” *Nature* **601**, 343 (2022).
- [12] A. Noiri, K. Takeda, T. Nakajima, T. Kobayashi, A. Sammak, G. Scappucci, and S. Tarucha, “Fast universal quantum gate above the fault-tolerance threshold in silicon,” *Nature* **601**, 338 (2022).
- [13] M. T. Mądzik, S. Asaad, A. Youssry, B. Joecker, K. M. Rudinger, E. Nielsen, K. C. Young, T. J. Proctor, A. D. Baczewski, A. Laucht *et al.*, “Precision tomography of a three-qubit donor quantum processor in silicon,” *Nature* **601**, 348 (2022).
- [14] A. R. Mills, C. R. Guinn, M. J. Gullans, A. J. Sigillito, M. M. Feldman, E. Nielsen, and J. R. Petta, “Two-qubit silicon quantum processor with operation fidelity exceeding 99%,” *Sci. Adv.* **8**, eabn5130 (2022).
- [15] R. Raussendorf and J. Harrington, “Fault-Tolerant Quantum Computation with High Threshold in Two Dimensions,” *Phys. Rev. Lett.* **98**, 190504 (2007).
- [16] A. G. Fowler, M. Mariantoni, J. M. Martinis, and A. N. Cleland, “Surface codes: Towards practical large-scale quantum computation,” *Phys. Rev. A* **86**, 032324 (2012).
- [17] T. Hensgens, T. Fujita, L. Janssen, X. Li, C. J. Van Diepen, C. Reichl, W. Wegscheider, S. Das Sarma, and L. M. K. Vandersypen, “Quantum simulation of a Fermi–Hubbard model using a semiconductor quantum dot array,” *Nature* **548**, 70 (2017).
- [18] J. P. Dehollain, U. Mukhopadhyay, V. P. Michal, Y. Wang, B. Wunsch, C. Reichl, W. Wegscheider, M. S. Rudner, E. Demler, and L. M. K. Vandersypen, “Nagaoka ferromagnetism observed in a quantum dot plaquette,” *Nature* **579**, 528 (2020).
- [19] M. Kiczynski, S. K. Gorman, H. Geng, M. B. Donnelly, Y. Chung, Y. He, J. G. Keizer, and M. Simmons, “Engineering topological states in atom-based semiconductor quantum dots,” *Nature* **606**, 694 (2022).
- [20] J. Preskill, “Quantum computing and the entanglement frontier,” *arXiv:1203.5813* (2012).
- [21] A. Laucht, R. Kalra, J. T. Muhonen, J. P. Dehollain, F. A. Mohiyaddin, F. Hudson, J. C. McCallum, D. N.

- Jamieson, A. S. Dzurak, and A. Morello, “High-fidelity adiabatic inversion of a ^{31}P electron spin qubit in natural silicon,” *Appl. Phys. Lett.* **104**, 092115 (2014).
- [22] T. Albash and D. A. Lidar, “Adiabatic quantum computation,” *Rev. Mod. Phys.* **90**, 015002 (2018).
- [23] X. Chen, I. Lizuain, A. Ruschhaupt, D. Guéry-Odelin, and J. G. Muga, “Shortcut to Adiabatic Passage in Two- and Three-Level Atoms,” *Phys. Rev. Lett.* **105**, 123003 (2010).
- [24] D. Guéry-Odelin, A. Ruschhaupt, A. Kiely, E. Torrontegui, S. Martínez-Garaot, and J. G. Muga, “Shortcuts to adiabaticity: Concepts, methods, and applications,” *Rev. Mod. Phys.* **91**, 045001 (2019).
- [25] Y. Ban, X. Chen, E. Y. Sherman, and J. G. Muga, “Fast and Robust Spin Manipulation in a Quantum Dot by Electric Fields,” *Phys. Rev. Lett.* **109**, 206602 (2012).
- [26] A. Baksic, H. Ribeiro, and A. A. Clerk, “Speeding up Adiabatic Quantum State Transfer by Using Dressed States,” *Phys. Rev. Lett.* **116**, 230503 (2016).
- [27] M. V. Berry, “Transitionless quantum driving,” *J. Phys. A: Math. Theor.* **42**, 365303 (2009).
- [28] T. Wang, Z. Zhang, L. Xiang, Z. Jia, P. Duan, W. Cai, Z. Gong, Z. Zong, M. Wu, J. Wu *et al.*, “The experimental realization of high-fidelity ‘shortcut-to-adiabaticity’ quantum gates in a superconducting Xmon qubit,” *New J. of Phys.* **20**, 065003 (2018).
- [29] W. Zheng, Y. Zhang, Y. Dong, J. Xu, Z. Wang, X. Wang, Y. Li, D. Lan, J. Zhao, S. Li *et al.*, “Optimal control of stimulated Raman adiabatic passage in a superconducting qubit,” *npj Quantum Inf.* **8**, 9 (2022).
- [30] B. B. Zhou, A. Baksic, H. Ribeiro, C. G. Yale, F. J. Heremans, P. C. Jerger, A. Auer, G. Burkard, A. A. Clerk, and D. D. Awschalom, “Accelerated quantum control using superadiabatic dynamics in a solid-state lambda system,” *Nat. Phys.* **13**, 330 (2017).
- [31] J. Zhang, J. H. Shim, I. Niemeyer, T. Taniguchi, T. Teraji, H. Abe, S. Onoda, T. Yamamoto, T. Ohshima, J. Isoya, and D. Suter, “Experimental Implementation of Assisted Quantum Adiabatic Passage in a Single Spin,” *Phys. Rev. Lett.* **110**, 240501 (2013).
- [32] M. G. Bason, M. Viteau, N. Malossi, P. Huillery, E. Arimondo, D. Ciampini, R. Fazio, V. Giovannetti, R. Mannella, and O. Morsch, “High-fidelity quantum driving,” *Nat. Phys.* **8**, 147 (2012).
- [33] Y.-X. Du, Z.-T. Liang, Y.-C. Li, X.-X. Yue, Q.-X. Lv, W. Huang, X. Chen, H. Yan, and S.-L. Zhu, “Experimental realization of stimulated Raman shortcut-to-adiabatic passage with cold atoms,” *Nat. Commun.* **7**, 12479 (2016).
- [34] E. Boyers, P. J. D. Crowley, A. Chandran, and A. O. Sushkov, “Exploring 2D Synthetic Quantum Hall Physics with a Quasiperiodically Driven Qubit,” *Phys. Rev. Lett.* **125**, 160505 (2020).
- [35] S. G. J. Philips, M. T. Mądzik, S. V. Amitonov, S. L. de Snoo, M. Russ, N. Kalhor, C. Volk, W. I. L. Lawrie, D. Brousse, L. Trypuzen *et al.*, “Universal control of a six-qubit quantum processor in silicon,” *Nature* **609**, 919 (2022).
- [36] K. C. Nowack, F. H. L. Koppens, Y. V. Nazarov, and L. M. K. Vandersypen, “Coherent Control of a Single Electron Spin with Electric Fields,” *Science* **318**, 1430 (2007).
- [37] X. Croot, X. Mi, S. Putz, M. Benito, F. Borjans, G. Burkard, and J. R. Petta, “Flopping-mode electric dipole spin resonance,” *Phys. Rev. Res.* **2**, 012006(R) (2020).
- [38] R. Hanson, B. Witkamp, L. M. K. Vandersypen, L. H. Willems van Beveren, J. M. Elzerman, and L. P. Kouwenhoven, “Zeeman Energy and Spin Relaxation in a One-Electron Quantum Dot,” *Phys. Rev. Lett.* **91**, 196802 (2003).
- [39] J. M. Elzerman, R. Hanson, L. H. Willems van Beveren, B. Witkamp, L. M. K. Vandersypen, and L. P. Kouwenhoven, “Single-shot read-out of an individual electron spin in a quantum dot,” *Nature* **430**, 431 (2004).
- [40] D. Keith, S. K. Gorman, L. Kranz, Y. He, J. G. Keizer, M. A. Broome, and M. Y. Simmons, “Benchmarking high fidelity single-shot readout of semiconductor qubits,” *New J. of Phys.* **21**, 063011 (2019).
- [41] C. Barthel, M. Kjærgaard, J. Medford, M. Stopa, C. M. Marcus, M. P. Hanson, and A. C. Gossard, “Fast sensing of double-dot charge arrangement and spin state with a radio-frequency sensor quantum dot,” *Phys. Rev. B* **81**, 161308(R) (2010).
- [42] D. J. Reilly, C. M. Marcus, M. P. Hanson, and A. C. Gossard, “Fast single-charge sensing with a rf quantum point contact,” *Appl. Phys. Lett.* **91**, 162101 (2007).
- [43] M. Shafiei, K. C. Nowack, C. Reichl, W. Wegscheider, and L. M. K. Vandersypen, “Resolving Spin-Orbit- and Hyperfine-Mediated Electric Dipole Spin Resonance in a Quantum Dot,” *Phys. Rev. Lett.* **110**, 107601 (2013).
- [44] C. Zener, “Non-adiabatic crossing of energy levels,” *Proc. R. Soc. A* **137**, 696 (1932).
- [45] C. Wittig, “The Landau-Zener Formula,” *J. Phys. Chem. B* **109**, 8428 (2005).
- [46] T. Nakajima, A. Noiri, K. Kawasaki, J. Yoneda, P. Stano, S. Amaha, T. Otsuka, K. Takeda, M. R. Delbecq, G. Allison, A. Ludwig, A. D. Wieck, D. Loss, and S. Tarucha, “Coherence of a Driven Electron Spin Qubit Actively Decoupled from Quasistatic Noise,” *Phys. Rev. X* **10**, 011060 (2020).
- [47] F. K. Malinowski, F. Martins, L. Cywiński, M. S. Rudner, P. D. Nissen, S. Fallahi, G. C. Gardner, M. J. Manfra, C. M. Marcus, and F. Kuemmeth, “Spectrum of the Nuclear Environment for GaAs Spin Qubits,” *Phys. Rev. Lett.* **118**, 177702 (2017).
- [48] E. J. Connors, J. Nelson, L. F. Edge, and J. M. Nichol, “Charge-noise spectroscopy of Si/SiGe quantum dots via dynamically-decoupled exchange oscillations,” *Nat. Commun.* **13**, 940 (2022).

and precisely tune the potentials of QDs. The bias-tees are connected with plunger gates P1 and P2, allowing for the application of MW and nano-second scale pulses. The barrier gates B1, B2, and B3 can be used to control the tunneling strength. An in-plane magnetic field $B_{\text{ext}} = 3.1$ T is applied, corresponding to the resonant frequency of single electron spin qubit $f_{\text{qubit}} \sim 18.0$ GHz. The RF-reflectometry provides rapid and real time detection of charge state. All the characterization and measurements are performed in a dilution refrigerator with the electron temperature around 140 mK. Note that there is also a cobalt micromagnet deposited on the surface of this device. However, we do not observe significant enhancement of the Rabi frequency for the rightmost DQDs used in this work.

The stability diagram of this DQDs system around the single electron charge configuration is shown in Fig. 1(b) of the main text. The number (n_L, n_R) stands for the electron occupation of the left and right QD. The electron is initialized to the spin $|\uparrow\rangle$ state at the position (I) based on the energy-selective tunneling. The tunneling in time T_{in}^{\uparrow} ($T_{\text{in}}^{\downarrow}$) of loading a spin $|\uparrow\rangle$ ($|\downarrow\rangle$) electron from the reservoirs is tuned around $2.64 \mu\text{s}$ ($14.1 \mu\text{s}$), along with the initialization fidelity estimated to be $F_{\text{ini}}^{\uparrow} \sim 98.8\%$. Then, plunger gates P1 and P2 provide nano-second scale pulse sequences to delivery this electron to an intermediate transit point (B) and then to the operation point (O). The EDSR is implemented by the application of the MW pulse, which is generated by the Keysight N5173B signal generator and I/Q modulated by the signals from the AWG Tektronix 5014B. The MW pulse is applied on the plunger gate P1 through one bias-tee and directional coupler. We employ energy-selective readout to measure the spin state at the readout (R) point, the same with the I point. Note that a detuning $\Delta\epsilon \sim -0.26 E_z$ (E_z is the Zeeman splitting) between the Fermi level and the center energy level of $|\downarrow\rangle$ and $|\uparrow\rangle$ states exists at the I and R position. At the readout position R, the tunneling out time $T_{\text{out}}^{\downarrow}$ ($T_{\text{out}}^{\uparrow}$) of the electron with spin $|\downarrow\rangle$ ($|\uparrow\rangle$) into reservoirs is tuned around $3.22 \mu\text{s}$ ($287.94 \mu\text{s}$). The spin to charge fidelity of $|\downarrow\rangle$ ($|\uparrow\rangle$) state is estimated to be $F_{\text{STC}}^{\downarrow} \sim 96.7\%$ ($F_{\text{STC}}^{\uparrow} \sim 93.9\%$). The electrical detection fidelity limited by the bandwidth of the RF-reflectometry is $F_E \sim 90.4\%$ for both $|\downarrow\rangle$ and $|\uparrow\rangle$ states [S1].

II. QUANTUM STATE TRANSFER UNDER TLQD, ADIABATIC EVOLUTION, AND ANTI-TLQD

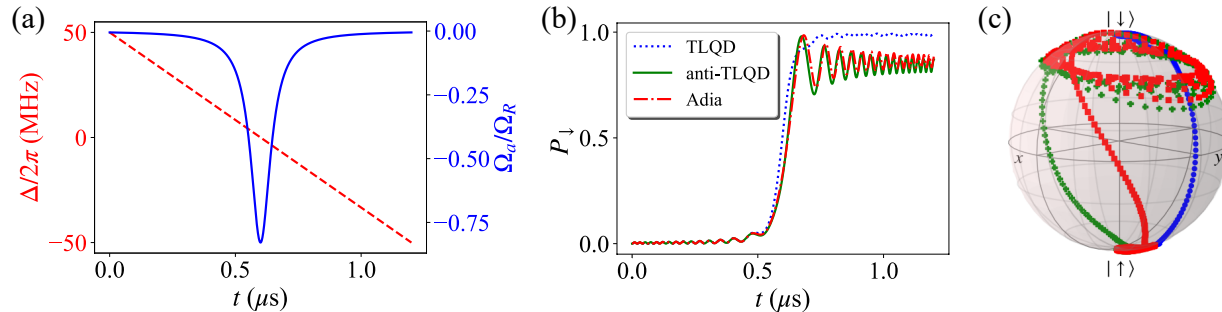


Figure S2. (a) Time dependent detuning $\Delta(t)$ and counter-diabatic driving $\Omega_a(t)$ when $\Omega_R/2\pi$ is kept as 4.0 MHz. The detuning Δ is modulated linearly, and Ω_a follows the Gaussian envelope based on its expression of previous results [S2]. (b) The spin down probability P_{\downarrow} as a function of the evolution time t . The blue dotted line, red solid line, and green dashdotted line correspond to TLQD ($\phi = 0$), adiabatic evolution ($\phi = \pi/2$), and anti-TLQD ($\phi = \pi$) situations, respectively. The TLQD can always keep the electron spin in its instantaneous eigenstate state. (c) The evolution of electron spin state in Bloch sphere. The blue circles, red squares, and green pluses represent TLQD, adiabatic evolution, and anti-TLQD, respectively.

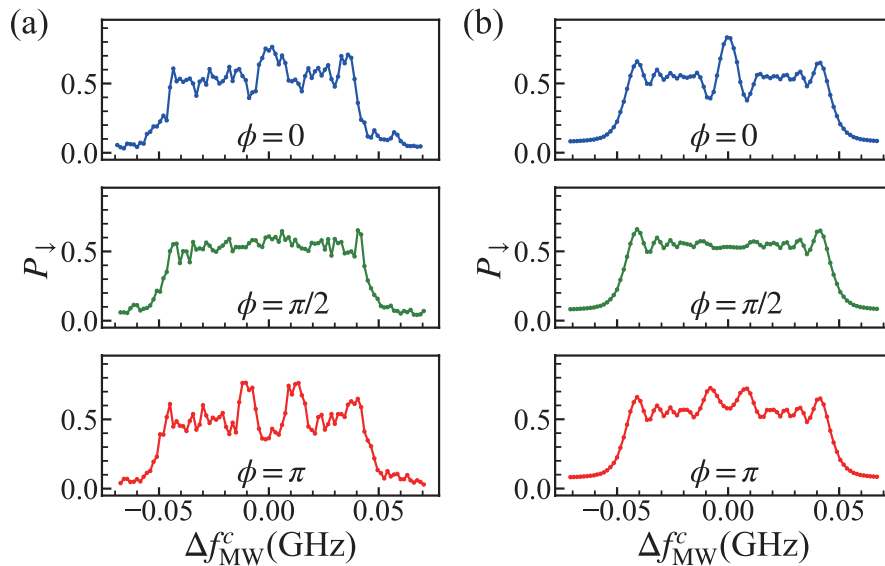


Figure S3. The experimental (a) and simulation (b) results of the spin down probability P_{\downarrow} as a function of the detuning Δf_{MW}^c . The Rabi frequency is $\Omega_R/2\pi = 3.44$ MHz. The modulation depth is $\delta_d = 100$ MHz, and the evolution time is $T_e = 0.6 \mu\text{s}$.

To better understand the basic principles and functions of the counter-diabatic term Ω_a , a phase ϕ is included, and the corresponding Hamiltonian becomes $\hat{H}_{\text{CD}} = \hbar\Omega_a \cos \phi \sigma_y/2$. The parameters $\phi = 0$, $\phi = \pi/2$, and $\phi = \pi$ correspond to the situations of TLQD, conventional adiabatic evolution, and anti-TLQD, respectively. The anti-TLQD means there is a π phase for this counter-diabatic term, i.e., $\Omega_a \rightarrow -\Omega_a$. The experimental data and simulation results of spin down probability P_{\downarrow} as a function of the detuning Δf_{MW}^c are shown in Fig. S3. In this figure, the MW frequency f_{MW} is linearly modulated from $f_{\text{MW}}^c - \delta_d/2$ to $f_{\text{MW}}^c + \delta_d/2$, in which f_{MW}^c is the center frequency of the MW. The detuning $\Delta f_{\text{MW}}^c = f_{\text{qubit}} - f_{\text{MW}}^c$ is the frequency difference between f_{qubit} and f_{MW}^c . For the TLQD ($\phi = 0$), P_{\downarrow} can reach the maximum value when $\Delta f_{\text{MW}}^c = 0$. In contrast, there is always a dip for the anti-TLQD ($\phi = \pi$), while it is flat for the adiabatic evolution ($\phi = \pi/2$). The results mean that the enhancement of state transfer originates from the compensation for diabatic errors instead of simply enlarging the Rabi frequency.

III. RABI OSCILLATION AND LANDAU-ZENER TRANSITION

The coherent Rabi oscillation provides a straight forward method to evaluate Ω_R (or Ω_a). As shown in Fig. S4(b), the Rabi frequency is estimated to be $f_{\text{Rabi}} (= \Omega_R/2\pi) \sim 4.1$ MHz after fitting to the formula $P_{\downarrow}(t) = A \exp(-t^2/T_{2,\text{Rabi}}^2) \cos(2\pi f_{\text{Rabi}} t_b) + B$. Another optional method to obtain f_{Rabi} is utilizing the Landau-Zener transition. For the implementation, the electron is initialized to spin up $|\uparrow\rangle$ state. Then, a linearly modulated MW pulse with the evolution time T_e and depth $\delta_d = 100$ MHz is applied. The probability of state transfer to the $|\downarrow\rangle$ state after this frequency modulation is described by the Landau-Zener formula

$$P_{\downarrow}^{\text{LZ}} = \exp\left(-\frac{\pi\Omega_R^2}{2\dot{\Delta}}\right). \quad (\text{S-1})$$

Here, the frequency modulation speed is $\dot{\Delta} = 2\pi\delta_d/T_e$. The value of Ω_R can be evaluated from the fitting to the above equation under various modulation time T_e . Figure S4(a) shows the exponential changes of $P_{\downarrow}^{\text{LZ}}$, giving the estimated value of $f_{\text{Rabi}} \sim 4.2$ MHz. The value of f_{Rabi} evaluated from the coherent Rabi oscillation and Landau-Zener transition are nearly the same.

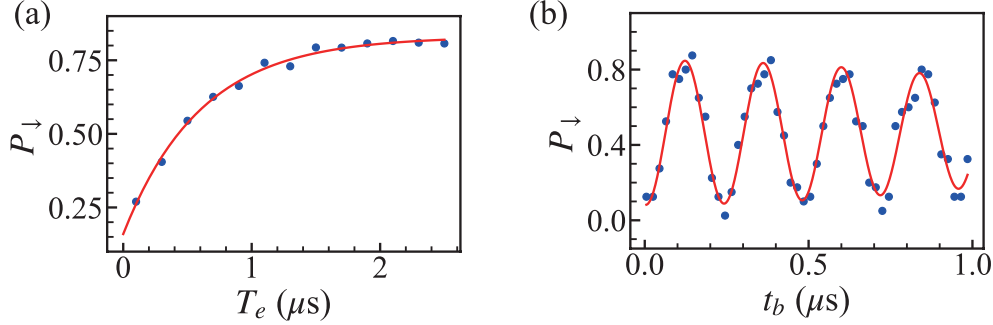


Figure S4. (a) The Landau-Zener transition graphic, i.e., the spin down probability P_{\downarrow} as a function of the evolution time T_e . The modulation depth δ_d is 100.0 MHz. The experimental value obtained from the fitting of $AP_{\downarrow}^{\text{LZ}} + B$ is $\Omega_R/2\pi \sim 4.2$ MHz. (b) Rabi oscillation. The voltage for the I/Q mixer is designed to make the same theoretical Ω_R value with (a). The red fitting curve gives $\Omega_R/2\pi \sim 4.1$ MHz.

IV. PULSE SEQUENCES

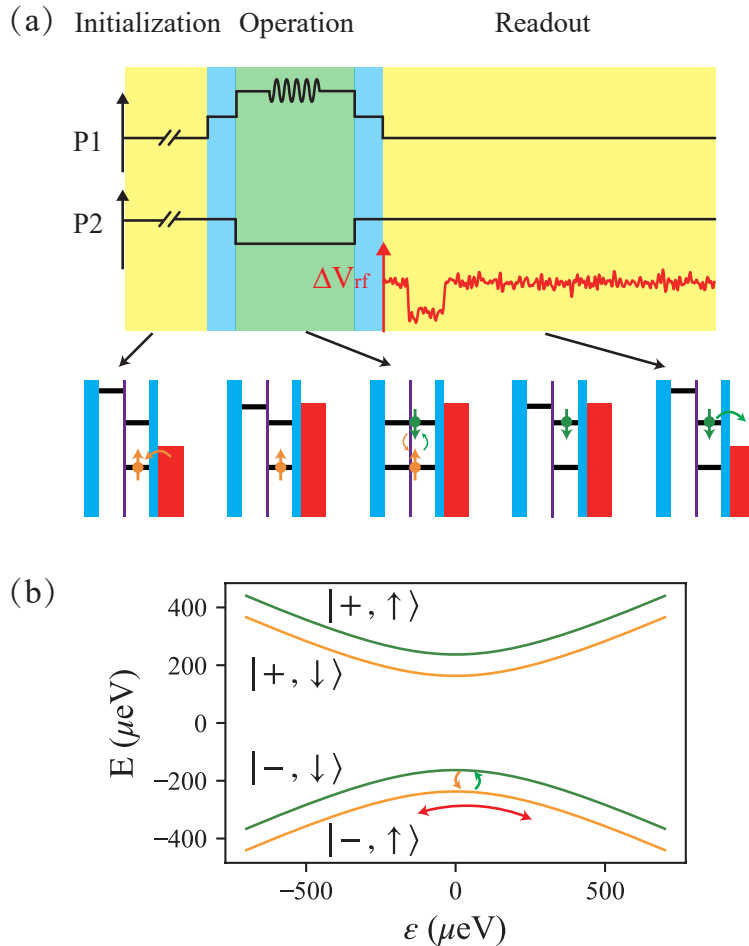


Figure S5. (a) The schematic of pulse sequences. The pulses are generated from the AWG Tektronix 5014B, then they are applied on the gates P1 and P2 through the high-frequency cables and bias-tees. The energy selective tunneling is used to readout the charge state [S3]. The red line of ΔV_{rf} is the trace of signals from the RF-reflectometry when the event of electron tunneling occurs during the readout. (b) The spectrum of DQDs around the zero energy detuning region. The single electron is shuttled between the left and right QD after applying the MW, so there is a quantum state transition between the $|-, \uparrow\rangle$ and $|-, \downarrow\rangle$ state.

In order to enhance the Rabi frequency, the operation point is chosen around the zero detuning region between the left and right QD [S4]. The Hamiltonian of this system after applying an in-plane magnetic field can be written as

$$\hat{H} = \frac{\epsilon}{2}\tau_z + t\tau_x + \frac{E_z}{2}\sigma_z, \quad (\text{S-2})$$

in which ϵ and t are the energy detuning and tunnel coupling between the left and right QD, respectively. τ_z and τ_x are Pauli matrixes expanded in the basis of $|L\rangle$ and $|R\rangle$, whose expressions are $\tau_z = |L\rangle\langle L| - |R\rangle\langle R|$ and $\tau_x = |L\rangle\langle R| + |R\rangle\langle L|$. The last term of the Hamiltonian describes the spin term, in which $\sigma_z = |\downarrow\rangle\langle\downarrow| - |\uparrow\rangle\langle\uparrow|$ and E_z is the Zeeman splitting.

Figure S5(b) shows the spectrum of the Hamiltonian in Eq. (S-2). In this experiment, the electron is shuttled between the left and right QD adiabatically to increase the spin-orbit interaction and Rabi frequency. The value of tunnel coupling t is larger than $200 \mu\text{eV}$ and the Zeeman splitting E_z is about $74 \mu\text{eV}$. The adiabatic shuttling

between left and right QD is determined by Landau-Zener formula

$$P_{\text{DQDs}}^{\text{LZ}} = \exp\left(\frac{-2\pi t^2}{\hbar \dot{\epsilon}}\right). \quad (\text{S-3})$$

Here, $\dot{\epsilon} \sim 2f_{\text{MW}}\delta\epsilon$. $\delta\epsilon$ is the change of the detuning and its value is less than 1000 μeV according to our rough estimation. Therefore, we can know that $P_{\text{DQDs}}^{\text{LZ}} \ll 1$ and the adiabatic condition can be satisfied.

V. NOISE SPECTRUM

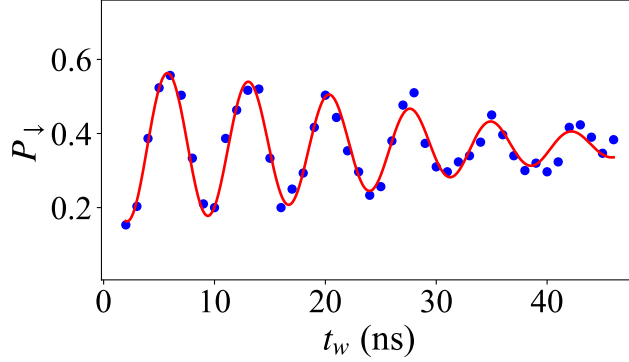


Figure S6. Ramsey oscillation. The red line is the fitting curve to the formula $P_{\downarrow}(t) = A + B \sin(2\pi f t_w + \phi) \exp[-(t_w/T_2^*)^2]$. The parameters after fitting are $f = 136.89$ MHz and $T_2^* = 33.2$ ns.

The noise spectrum can be extracted from the free-induction decay (FID). Generally, the decay envelope of the phase is dominated by the long corrected noises [S5, S6]. It is often nonexponential and can be characterized by the factor $W(t)$. For example, $W(t)$ describing the dephasing caused by the Gaussian noise is

$$W(t) = \exp\left(-\frac{t^2}{2} (2\pi)^2 \int_{-\infty}^{\infty} df S_L(f) \text{sinc}^2(\pi f t)\right). \quad (\text{S-4})$$

Here, $\text{sinc}(x) = \sin x/x$. Since the longitudinal relaxation time is much longer than the pure transverse relaxation time, the dephasing caused by longitudinal relaxation can be neglected. The envelope decay is mainly dominated by the quasistatic noise, i.e., $|f| < 1/t$. Meanwhile, $\text{sinc}(\pi f t) \approx 1$ if $|f| \ll 1/t$. Therefore, this envelope follows the Gaussian decay with the expression as

$$E_{\text{free}}(t) = \exp\left[-\left(\frac{t}{T_2^*}\right)^2\right] = \exp\left[-\frac{t^2}{2} (2\pi\sigma)^2\right]. \quad (\text{S-5})$$

Here, $\sigma = 2 \int_{f_c}^{1/t} S_L(f) df$, in which f_c is the lower cut-off frequency. The relationship between the T_2^* and the variance of the qubit frequency is $T_2^* = 1/(\sqrt{2}\pi\sigma)$. For the GaAs semiconductor QDs, the quasistatic noise is dominated by the Overhauser field, and the two-sided power spectrum is $S(f) = A^2/f^2$. The coherence time T_2^* extracted from the FID (or Ramsey oscillation) is

$$1/T_2^* = 2\pi A \sqrt{1/f_c - t}. \quad (\text{S-6})$$

Figure S6 shows the Ramsey oscillation with the lower cut-off frequency $f_c \sim 0.71$ Hz, giving the value of $A \sim 4.043 \times 10^6 \text{ Hz}^{\frac{3}{2}}$.

The variance of the qubit frequency σ is different in Fig. 2(a) and Fig. 3(a) of the main text, which is mainly due to the different value of f_c . In our experiment, we load all the waveform under different T_e (or α) to the AWG simultaneously. In Fig. 2(a), each one single-shot measurement under different T_e ranging from $0.15 \mu\text{s}$ to $1.45 \mu\text{s}$ is performed in serious. This process is repeated until we finish the measurement. Therefore, the value of $1/f_c$ is set to be the total measurement time. We can also know the value of σ using the same method for Fig. 3(a) under different α .

VI. INITIALIZATION AND READOUT FIDELITY

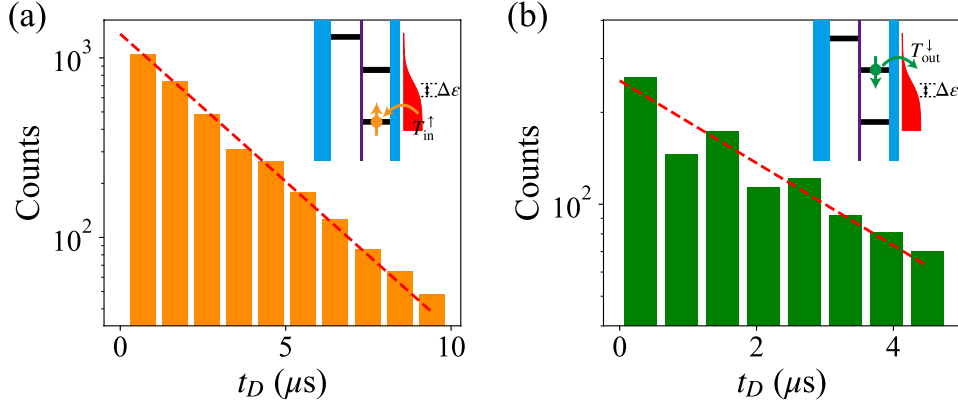


Figure S7. Histogram showing the tunneling in time T_{in}^{\uparrow} of $|\uparrow\rangle$ state (a) and tunneling out time $T_{\text{out}}^{\downarrow}$ of $|\downarrow\rangle$ state (b), whose values are $2.64 \mu\text{s}$ and $3.22 \mu\text{s}$, respectively.

This section will introduce the method used for the analyses of state preparation and measurement (SPAM). The following analyses of fidelity and naming scheme are proposed by D. Keith *et al.* in the paper “New Journal of Physics **21**, 063011 (2019)” [S1]. Here, we use their method and naming scheme to analyze the properties of our sample.

The readout fidelity of $|\uparrow\rangle$ and $|\downarrow\rangle$ state are analyzed firstly. The loading time T_{in}^{\uparrow} of the $|\uparrow\rangle$ state and tunneling out time $T_{\text{out}}^{\downarrow}$ of the $|\downarrow\rangle$ state can be measured directly, as shown in Fig. S7. The values of T_{in}^{\uparrow} and $T_{\text{out}}^{\downarrow}$ extracted from the histograms are $2.64 \mu\text{s}$ and $3.22 \mu\text{s}$, respectively. We find that the Fermi level E_F of the reservoirs is not in the center position of the $|\uparrow\rangle$ and $|\downarrow\rangle$ state, which means that a detuning $\Delta\epsilon$ exists. Its value can be estimated from the following relationship

$$\frac{T_{\text{out}}^{\downarrow}}{T_{\text{in}}^{\uparrow}} = \frac{f(\Delta\epsilon - E_z/2)}{1 - f(\Delta\epsilon + E_z/2)}. \quad (\text{S-7})$$

Here, $f(\epsilon)$ is the Fermi–Dirac distribution with the expression $f(\epsilon) = [1 + \exp(\epsilon/k_B T)]^{-1}$. E_z is the Zeeman splitting after applying the in-plane magnetic field. k_B is the Boltzmann constant. The electron temperature is $T \sim 140 \text{ mK}$. The value of this detuning is $\Delta\epsilon \sim -0.26 E_z$. Furthermore, the tunneling out time $T_{\text{out}}^{\uparrow}$ of the $|\uparrow\rangle$ state and the loading time $T_{\text{in}}^{\downarrow}$ of the $|\downarrow\rangle$ state are estimated to be $287.94 \mu\text{s}$ and $14.12 \mu\text{s}$, respectively. This estimation is based on the relationship

$$\frac{T_{\text{in}}^{\uparrow}}{T_{\text{in}}^{\downarrow}} = \frac{f(\Delta\epsilon + E_z/2)}{f(\Delta\epsilon - E_z/2)}, \quad \text{and} \quad \frac{T_{\text{out}}^{\uparrow}}{T_{\text{out}}^{\downarrow}} = \frac{1 - f(\Delta\epsilon + E_z/2)}{1 - f(\Delta\epsilon - E_z/2)}. \quad (\text{S-8})$$

The spin-to-charge fidelity can be calculated using the following formula

$$F_{\text{STC}}^{\uparrow} = e^{-\frac{t}{T_{\text{out}}^{\uparrow}}},$$

$$F_{\text{STC}}^{\downarrow} = \frac{1}{T_{\text{out}}^2} \left[\left(1 - e^{-\frac{t}{T_{\text{out}}^{\uparrow}}}\right) T_{\text{out}}^{\uparrow} T_{\text{out}}^{\downarrow} + \left(e^{-\frac{T_1 + T_{\text{out}}^{\downarrow}}{T_{\text{out}}^{\uparrow} T_1} t} - 1\right) T_1 (T_{\text{out}}^{\downarrow} - T_{\text{out}}^{\uparrow}) \right]. \quad (\text{S-9})$$

in which $T_{\text{out}}^2 = T_1 (T_{\text{out}}^{\uparrow} - T_{\text{out}}^{\downarrow}) + T_{\text{out}}^{\uparrow} T_{\text{out}}^{\downarrow}$. The relaxation time of the spin down state $|\downarrow\rangle$ is $T_1 \sim 99.5 \mu\text{s}$, as shown in Fig. S8(a). The readout time is about $18.0 \mu\text{s}$. Therefore, the values of $F_{\text{STC}}^{\downarrow}$ and $F_{\text{STC}}^{\uparrow}$ are 96.7% and 93.9%, respectively.

The total readout fidelity is also determined by the electrical detection fidelity, limited by the signal-to-noise ratio (SNR), bandwidth of the RF-reflectometry, and the sampling rate of the digitizer. Figure S9 shows the histogram of signals from the RF-reflectometry. If the threshold determining the tunneling out event is set at the center position

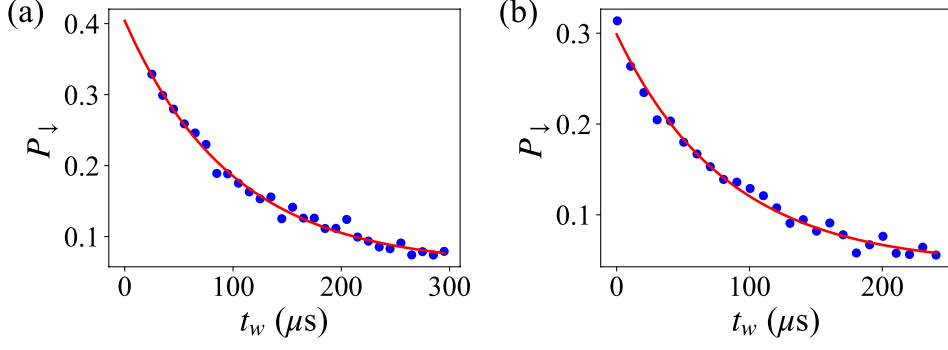


Figure S8. The relaxation time T_1 of the spin down $|\downarrow\rangle$ state at the R point (a) and O point (b). The fitting values of T_1 in (a) and (b) are $99.5 \mu\text{s}$ and $83.3 \mu\text{s}$, respectively.

of two Gaussian envelopes. The infidelity is less than 0.01%, meaning the SNR is high enough. The corresponding infidelity is neglected in the following analyses. Therefore, the electrical detection fidelity is only determined by the probability of missing the “fast blip”, which means that one electron tunnels out and another electron tunnels into the QDs quickly within the resolution time of the setup. In our experiment, the sampling rate of the digitizer is 10.0 MHz, and the bandwidth of the RF-reflectometry is 1.9 MHz. This “fast blip” occurs within the time $t_s \sim 0.53 \mu\text{s}$.

The tunneling out probability density of $|\uparrow\rangle$ and $|\downarrow\rangle$ state within the time t_s is

$$p_{\text{out}}^{\downarrow(\uparrow)}(t) = \frac{e^{-t/T_{\text{out}}^{\downarrow(\uparrow)}}}{T_{\text{out}}^{\downarrow(\uparrow)}(1 - e^{-t_s/T_{\text{out}}^{\downarrow(\uparrow)}})}, \quad 0 < t < t_s. \quad (\text{S-10})$$

The tunneling in probability density of $|\uparrow\rangle$ state after the tunneling out of one electron is

$$p_{\text{in}}^{\uparrow}(t) = \frac{e^{-t/T_{\text{in}}^{\uparrow}}}{T_{\text{in}}^{\uparrow}}. \quad (\text{S-11})$$

Therefore, the probability of missing the detection signal of tunneling out $|\uparrow\rangle$ or $|\downarrow\rangle$ state is

$$P_{\text{miss}}^{\downarrow(\uparrow)}(t) = \int_0^{t_s} \int_0^t p_{\text{out}}^{\downarrow(\uparrow)}(t - \tau) p_{\text{in}}^{\uparrow}(\tau) d\tau dt. \quad (\text{S-12})$$

From this calculation, we know the electrical charge detection fidelity of the $|\downarrow\rangle$ state and $|\uparrow\rangle$ state are 90.4% and state 90.6%, respectively.

Finally, we calculate the initialization fidelity of the spin up $|\uparrow\rangle$ state. The rate equation during the initialization stage is $d(P_0, P_{\uparrow}, P_{\downarrow})^T/dt = \mathbf{M}(P_0, P_{\uparrow}, P_{\downarrow})^T$. Here, P_0 , P_{\uparrow} , and P_{\downarrow} represent the probability of no electron, one electron with spin up, and one electron with spin down in the DQDs, respectively. The expression of \mathbf{M} is

$$\mathbf{M} = \begin{pmatrix} -\frac{1}{T_{\text{in}}^{\uparrow}} - \frac{1}{T_{\text{in}}^{\downarrow}} & \frac{1}{T_{\text{out}}^{\uparrow}} & \frac{1}{T_{\text{out}}^{\downarrow}} \\ \frac{1}{T_{\text{in}}^{\uparrow}} & -\frac{1}{T_{\text{out}}^{\uparrow}} & \frac{1}{T_1} \\ \frac{1}{T_{\text{in}}^{\downarrow}} & 0 & -\frac{1}{T_{\text{out}}^{\downarrow}} - \frac{1}{T_1} \end{pmatrix}. \quad (\text{S-13})$$

The initialization time is $30 \mu\text{s}$. If the initial state of the QDs is empty, the initialization fidelity of the spin up $|\uparrow\rangle$ state is $F_{\text{ini}}^{\uparrow} = P_{\uparrow}(t = 30\mu\text{s}) \sim 98.8\%$.

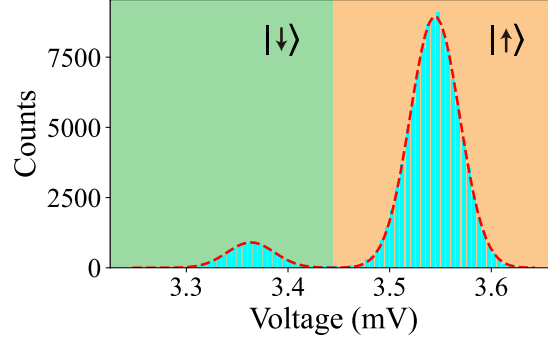


Figure S9. Histogram of the demodulated RF signals at the R point. The red dashed line is the double Gaussian fitting. This distribution corresponds to the infidelity of less than 0.01%, which can be neglected.

VII. THE RESULTS OF TLQD UNDER DIFFERENT Ω_R

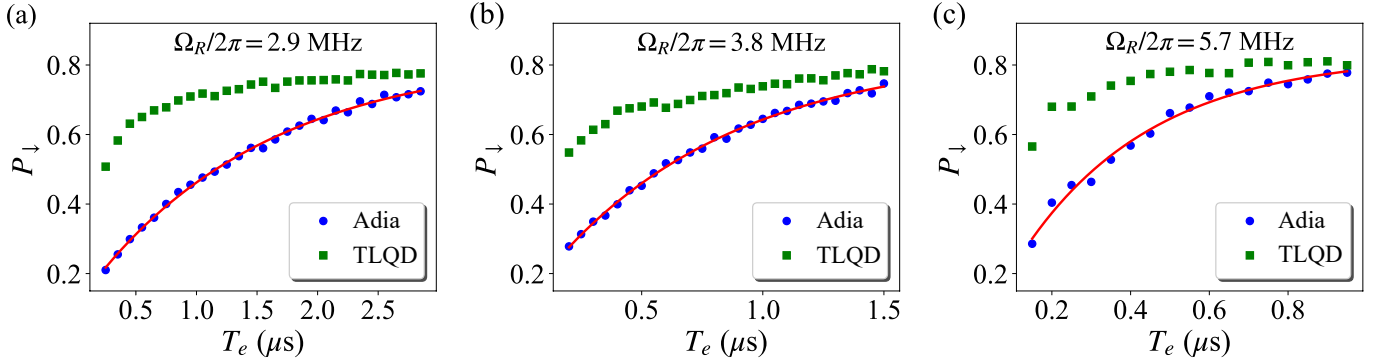


Figure S10. The spin down probability P_{\downarrow} as a function of the total evolution time T_e under different Ω_R . The blue circles and green squares correspond to the adiabatic evolution and TLQD, respectively. The red lines are the fitting results using the Landau-Zener formula.

VIII. PULSE OPTIMIZATION

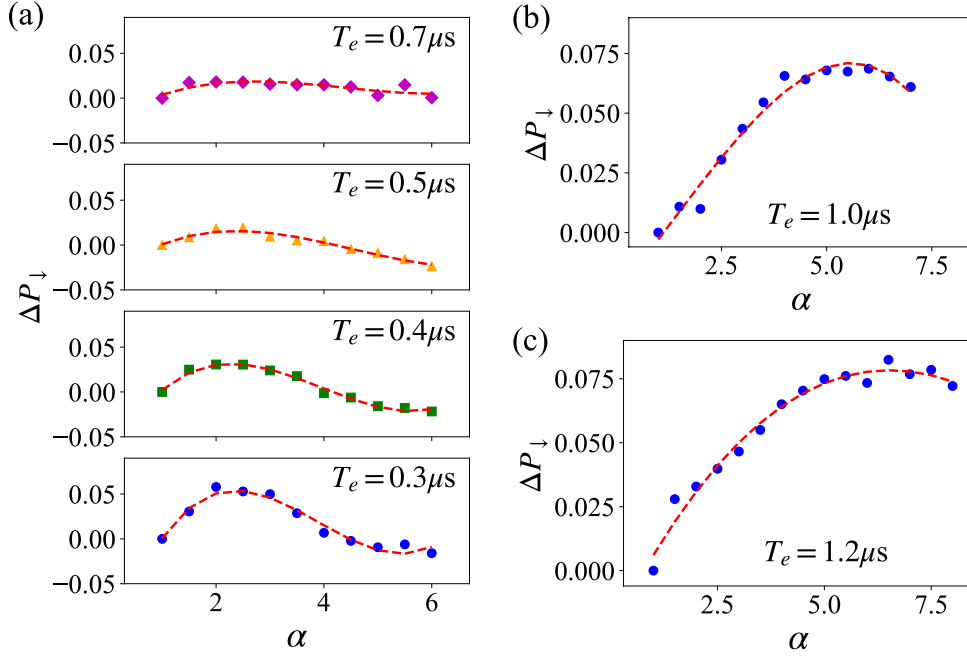


Figure S11. The width factor α dependence of ΔP_{\downarrow} . The values of Ω_R in (a), (b), and (c) are 4.8 MHz, 2.9 MHz, and 2.4 MHz, respectively. The red dashed lines are the polynomial fitting curves. The optimal width factor α are about 2.0 (a), 5.5 (b), and 6.5 (c), respectively. Generally, this optimal value becomes smaller with larger Ω_R .

IX. THE BENCHMARKING OF SPIN FLIP FIDELITY

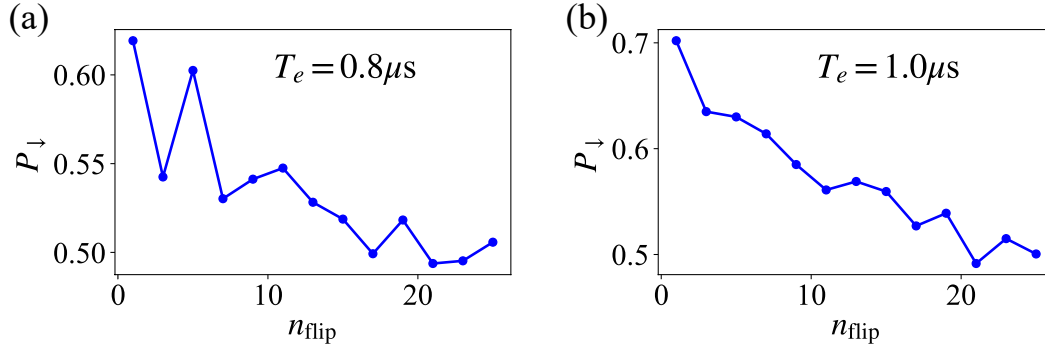


Figure S12. (a) and (b) show the spin down probability P_{\downarrow} as a function of spin flip number n_{flip} using the conventional adiabatic evolution when the total evolution time T_e are $0.8 \mu\text{s}$ and $1.0 \mu\text{s}$, respectively. When the T_e is short, e.g., $0.8 \mu\text{s}$, P_{\downarrow} can not show exponential decay, indicating the F_{flip} is very small. P_{\downarrow} start to follow an exponential decay when T_e is long enough. This is completely different from the TLQD theory, which can always exhibit exponential decay, even though T_e is very short.

X. THE RESULTS OF TLQD WITHOUT THE SATURATION OF RABI FREQUENCY

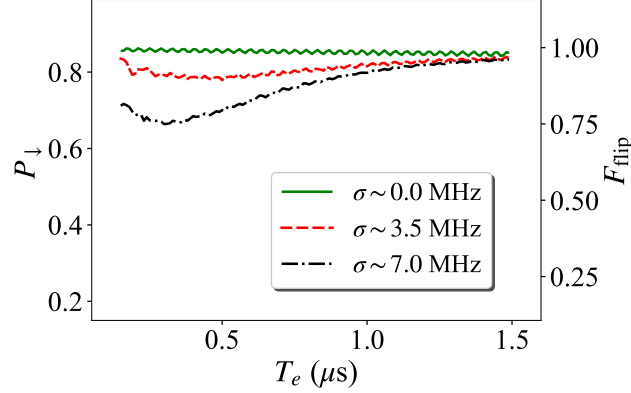


Figure S13. The simulation results of the spin down probability P_{\downarrow} and the state transfer efficiency F_{flip} of the TLQD scheme without considering the saturation of Rabi frequency.

-
- [S1] D. Keith, S. K. Gorman, L. Kranz, Y. He, J. G. Keizer, M. A. Broome, and M. Y. Simmons, “Benchmarking high fidelity single-shot readout of semiconductor qubits,” *New J. of Phys.* **21**, 063011 (2019).
 - [S2] X. Chen, I. Lizuain, A. Ruschhaupt, D. Guéry-Odelin, and J. G. Muga, “Shortcut to Adiabatic Passage in Two- and Three-Level Atoms,” *Phys. Rev. Lett.* **105**, 123003 (2010).
 - [S3] J. M. Elzerman, R. Hanson, L. H. Willems van Beveren, B. Witkamp, L. M. K. Vandersypen, and L. P. Kouwenhoven, “Single-shot read-out of an individual electron spin in a quantum dot,” *Nature* **430**, 431 (2004).
 - [S4] X. Croot, X. Mi, S. Putz, M. Benito, F. Borjans, G. Burkard, and J. R. Petta, “Flopping-mode electric dipole spin resonance,” *Phys. Rev. Res.* **2**, 012006(R) (2020).
 - [S5] T. Nakajima, A. Noiri, K. Kawasaki, J. Yoneda, P. Stano, S. Amaha, T. Otsuka, K. Takeda, M. R. Delbecq, G. Allison, A. Ludwig, A. D. Wieck, D. Loss, and S. Tarucha, “Coherence of a Driven Electron Spin Qubit Actively Decoupled from Quasistatic Noise,” *Phys. Rev. X* **10**, 011060 (2020).
 - [S6] F. K. Malinowski, F. Martins, L. Cywiński, M. S. Rudner, P. D. Nissen, S. Fallahi, G. C. Gardner, M. J. Manfra, C. M. Marcus, and F. Kuemmeth, “Spectrum of the Nuclear Environment for GaAs Spin Qubits,” *Phys. Rev. Lett.* **118**, 177702 (2017).